Computational Condensed Matter 26 (2021) e00538

Contents lists available at ScienceDirect

Computational Condensed Matter

journal homepage: http://ees.elsevier.com/cocom/default.asp

On the electronic properties of defective graphene buffer layer on 6H−SiC(0001)

C. Pereyra Huelmo*, Federico Iribarne, Pablo A. Denis

Laboratorio de Nanotecnología Computacional, Área Matemática, DETEMA, Facultad de Química, Universidad de la República, Montevideo, Uruguay

ARTICLE INFO

Article history:
Received 13 November 2020
Received in revised form
14 January 2021
Accepted 16 January 2021

Keywords:
Graphene buffer layer
Silicon carbide
Electronic properties
DFT calculations
Defects

ABSTRACT

Using first-principles calculations we predict that the electronic properties of graphene buffer layer (BL) on silicon carbide (SiC) can be modified by defect-induced itinerant states. Band structures and effective masses of single vacancy (SV), divacancy (DV) and Stone-Wales (SW) defective BL were calculated. Structural reconstruction at the vicinity of defects as well as spin polarization of silicon dangling bonds in the top bilayer SiC and nearby carbons from the BL, give rise to energetically degenerate magnetic states displaying electronic properties completely apart. This is particularly true for the SW and SV defective models where as many as three different magnetic states, turned out to be degenerate, either displaying a semiconductor nature or becoming half-metallic or even metallic. This is in contrast with previously reported results for the perfect BL (PBL) which suggested that most stable degenerate magnetic configurations share a semiconductor nature. On the other hand, for the DV system, the introduction of two vacancies in the BL causes loss of magnetism whereas a band gap of 0.54 eV is opened. Hole effective masses decay upon removal of one and two carbon atoms in the SV and DV systems where an increase in mobility is conceivable, provided current direction is carefully selected.

1. Introduction

Graphene is a two-dimensional carbon material with a hexagonal honeycomb lattice, whose band structure was initially calculated long before this most intriguing material was isolated and characterized [1]. The upper π* band and the lower π band share a linear dependence at the Dirac points in reciprocal space. As a consequence of these features, electrons in graphene behave as massless, chiral, Dirac fermions which travel at very rapid speed. Owing to some fascinating properties, such as ultra-high carrier mobility, superior electrical and thermal conductivities, graphene is amongst the most promising materials for future high-speed electronics, photonics, and biodevices [2–6]. Epitaxial graphene growth on silicon carbide (SiC) is the only technique available capable of spawning large-scale single-crystalline graphene directly on the insulating substrate [7,8]. This kind of growth is characterized by the presence of an interfacial layer, the so called graphene buffer layer (BL), consisting of carbon atoms with sp^2 and sp^3 hybridization, the latter covalently bonded to silicon atoms of the SiC top layer. Si atoms in this layer, not bonded to the BL, exhibit dangling bonds (DB) and, as previously demonstrated in our studies [9], they are capable of inducing characteristic antiferromagnetic (AF) configurations on the SiC-BL system, degenerate with the ferromagnetic state M = 4 μB. The spin-up and spin-down channels in the AF state are nearly degenerate and this state displays an indirect band gap of about 0.2 eV. For the M = 4 μB configuration, a gap of up to 2 eV (in the spin-down channel) may be opened [9].

The electronic properties of graphene-based materials can be considerably enriched by chemical modifications, including substitution [10–15] and molecular doping [16–19] as well as functionalization [20,21]. Another approach to tune graphene's properties is provided by ion or electron beam irradiation which introduces structural defects in the lattice [22–25]. In concrete, vacancies, impurities, and topological defects can be distinguished. Whilst in a vacancy defect one or more atoms are removed from the lattice, an impurity defect implies that one carbon atom is replaced by another atom of a different element. Finally, in a topological defect, no atom is removed from the lattice but the bonding angles

* Corresponding author.
E-mail address: cpereyra@fq.edu.uy (C. Pereyra Huelmo).

https://doi.org/10.1016/j.cocom.2021.e00538
2352-2143/

between the carbon atoms are rotated. Vacancy defects in graphene do not happen easily. The energy required to sputter a single atom out of the lattice is 18–20 eV [26] and the formation energy of a single vacancy in free-standing graphene is in the range of 7.2–8.6 eV [27–29]. However, the corresponding formation energy in the BL is three times lower (some 2.2 eV) [30], suggesting that the SiC substrate acts as a strong stabilizer for this type of defects.

Single vacancies migrate easily across the graphene plane and are stabilized when they coalescence to produce a divacancy defect [31–33]. In turn, the Stone-Wales defect is a common topological transformation which consists in a 90° rotation of a carbon-carbon bond, bringing about the formation of two heptagons connected with two pentagons.

Sometimes, the effect of structural defects is beneficial. For example, defects are essential in chemical and electrochemical studies, where they create preferential bonding sites for adsorption of atoms and molecules, useful for gas and liquid sensing [34,35]. In particular for graphene, reconstructed vacancies serve as efficient trapping centers for metal atoms, which can be used for engineering the local electronic and magnetic structure of the material [33,36]. Furthermore, the existence of defects in the graphene network would create diffusion channels facilitating the intercalation of atoms between the BL and the substrate [37,38]. At the same time, structural defects were shown to prominently modify the electronic band structure of free-standing graphene [39,40]. In effect, they may promote localized and sharp resonant states at Fermi energy, act as scattering centers for electrons and thus reduce, in a remarkably fashion, the electrical conductivity [41,42]. Although this is the general rule, there are also some exceptions whereby defects can be engineered in regular arrays to generate metallic or insulating states [43,44].

Recent theoretical work by us [30], which concerned an exhaustive study of the structural and magnetic properties of defective SiC-BL systems, revealed that the most stable configuration with a single vacancy (SV) (Fig. 1a) resulted from the removal of a sp^3 carbon atom in the BL. This model possesses a stable AF state even though it is almost degenerate with the M = 1 μ_B and the non-magnetic (NM) configurations: the energy differences between the AF configuration and the M = 1 μ_B and NM configurations (28 and 34 meV, respectively) are very close to the thermal energy at room temperature (26 meV), at the vdW-DF/DZP level of theory. The spin-density distribution is quite different from the one previously reported for the perfect BL, albeit some degree of degeneracy with other magnetic states was noted. For the system with two vacancies, the largest stabilization was attained when two neighboring sp^2 carbons were removed from the lattice hence forming a divacancy (DV) (Fig. 1b). The NM configuration was the lowest in energy for this model. Finally, in the case of the Stone-Wales defect in the BL (SW), the arrangement where one of the four Si DBs existing in the perfect SiC-BL lies beneath a pentagon of carbon atoms (Fig. 1c) was the most stable geometry. The M = 2 μ_B state proved to be the most stable for this model, yet almost degenerate with the AF configuration which lies 0.024 eV below the former. Moreover, the formerly reported [30] binding energies for the most stable models with one and two vacancies and with a Stone-Wales defect (−0.25, −0,18 and −0.25 eV/atom, respectively, at the vdW-DF level of theory) suggest a stable binding in each case, even more stable as compared with the non-defective system (−0.14 eV/atom) [9].

In addition to modifying the magnetic properties of the SiC-BL system, it is expected that the presence of defects would also cause important modifications in the electronic properties of the BL

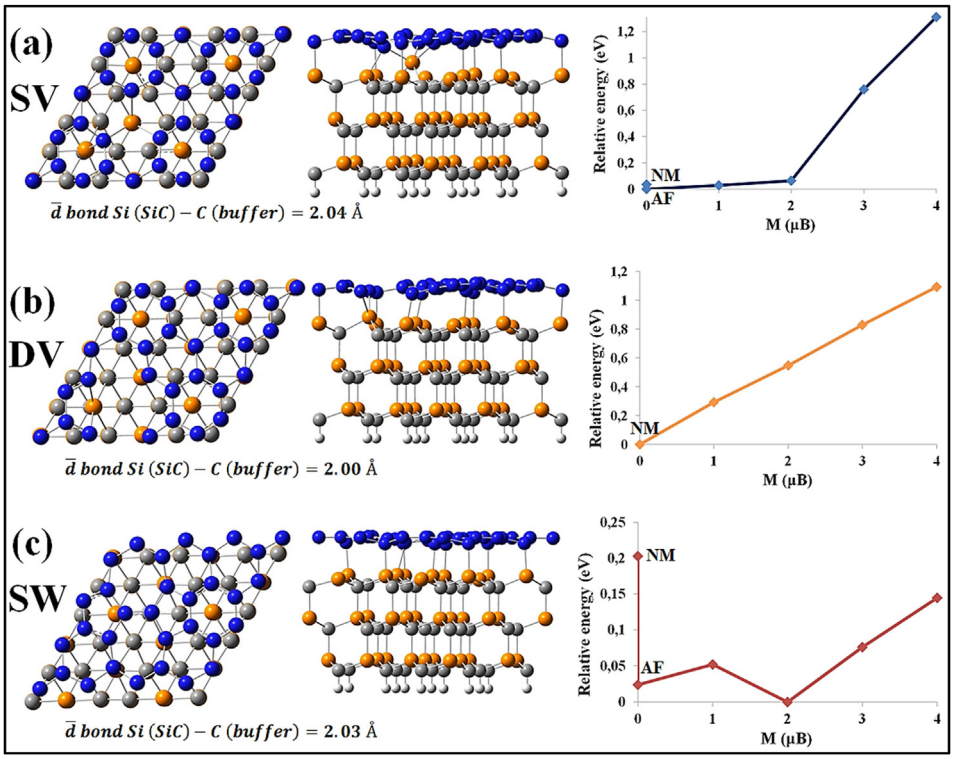

Fig. 1. (Left and center) Top and side views of optimized unit cells for the most stable 4 × 4 BL defective models on 6H−SiC(0001) previously reported in Ref. [30]: (a) single vacancy, (b) divacancy and (c) Stone-Wales defect. Carbon, silicon and hydrogen atoms in SiC are colored in grey, yellow and white, respectively. Carbon atoms in BL are colored in blue. (Right) Plot of relative energies versus magnetic moments, computed at the vdW-DF/DZP level of theory. NM: non-magnetic, AF: antiferromagnetic. (For interpretation of the references to color in this figure legend, the reader is referred to the Web version of this article.)

layer. As a continuation of this study, our intention now is to unravel the electronic properties of the SiC-BL defective systems as well as to provide a full comparison with the previously reported [9] properties for the non-defective one.

Herein, by means of density functional theory (DFT) calculations, we explore the electronic properties of the SiC-BL system with Stone-Wales, single vacancy and divacancy defects on the BL. In what follows, the most important results of the investigation are thoroughly presented and discussed, emphasizing the differences found in regard the electronic nature of the defective and the perfect BL systems. Understanding the electronic and magnetic properties that arise as a consequence of the complex interfacial atomic interactions in the SiC-BL system is fundamental if we want to take full advantage of the epitaxial growth of graphene in electronics, photonics or catalysis.

2. Methods

We carried out spin polarized vdW-DF calculations [45] as implemented in the SIESTA code [46,47]. Although expensive, the use of this functional is key to reproduce accurately the complex interactions of the interface and, in turn, the magnetic configuration of the SiC-buffer layer model. In this respect, a previously reported comparative study [9] suggests that vdW-DF would explain SQUID results and spin transport experiments with epitaxial graphene, when other functionals fail. Besides, Hamada and Otani recommended the use of the vdW-DF functional to study graphene deposited on substrates [48].

We selected the double-zeta basis set with polarization functions (DZP) and the orbital-confining cutoff was fixed to 0.01 Ry. The split norm used was 0.15. The interaction between ionic cores and valence electrons was described by Troullier-Martins norm conserving pseudopotentials [49]. The mesh cutoff was fixed to 200 Ry, which gave converged binding energies within 0.02 eV. Lattice parameters were fully optimized for all defective systems. The Brillouin zone was sampled in the reciprocal space using a Monkhorst-Pack k-point sampling scheme of $30 \times 30 \times 1$ k points. Further increase of the density of k points did not change the results. Band structures were calculated along the $\Gamma - M - K - \Gamma - M' - K' - \Gamma - M' - K' - \Gamma$ path. Geometry optimizations were pursued using the conjugate gradient algorithm until all residual forces were smaller than 0.01 eV/Å. During relaxation, we allowed for both fixed and variable magnetic moments. According to previous experience [9,12,14,15,28,30,50,51], SIESTA describes in an accurate manner the total energy, magnetic moments and electronic properties of graphene-based systems.

The BL consisted of an 8% stretched 4×4 graphene unit cell over a $\sqrt{3} \times \sqrt{3}$ rotated 30° 6H—SiC Si terminated unit cell. It has been demonstrated that the structure and magnetic properties obtained with six and eight layers can be likened to the ones found using three layers [9,52]. Given this background, we have built the substrate using three SiC layers having the C atoms at the bottom passivated by H atoms. Additionally, the strain of the $\sqrt{3} \times \sqrt{3}$ rotated 30° cell does not appear to have any qualitative effect on the fundamental properties of graphene as shown by Ridene et al. [53]. In spite of the fact that the $\sqrt{3} \times \sqrt{3}$ rotated 30° SiC unit cell is a simplification of the experimentally more frequently encountered $6\sqrt{3} \times 6\sqrt{3}$ rotated 30° SiC unit cell, it was shown that the former is stable, provides a consistent picture of the bonding in the interface zone [54], correctly captures the Clar sextets pattern and holds true in the valley regions of the BL [55–58]. In the same vein, the use of a 4×4 graphene unit cell to successfully study single and double vacancies has been reported [28,30]. Last but not least, the use of a smaller cell permits us to use the expensive vdW-DF density functional and also to consider spin polarization, which is essential to study the magnetic properties of the BL.

3. Results and discussion

Henceforth, all results will involve the defective models above described and presented in Fig. 1. The emphasis is put on the most stable magnetic states though the less stable magnetic states are also discussed for each defective system. For more specifics on structural and magnetic antecedents the reader is referred to Ref. [30].

To assess the electronic features of the SV, DV and SW defective interfaces, band structures have been calculated by a density functional approach considering different magnetic configurations, namely M = 4 μ_B, M = 3 μ_B, M = 2 μ_B, M = 1 μ_B, AF (if applicable), together with the NM state. Results are depicted in Figs. 2–4 and will be discussed in full detail in the next subsections.

Band gaps calculated at the vdW-DF/DZP level of theory are compiled in Table 1. For comparative purposes, data previously reported [9] for the perfect SiC-BL system (PBL) is included in the table.

3.1. BL with a single vacancy defect

For the SV system, the AF configuration is a semiconductor with a virtually zero indirect band gap at the spin-up channel and a larger indirect band gap at the spin-down channel (0.25 eV), as can be seen in Fig. 2a. This means that the SV defect breaks the nearly degeneracy existing for PBL in the AF configuration, which exhibited a band gap of 0.19 eV for both channels.

With the aim of understanding the orbital contribution in the bands close to the Fermi energy, projected density of states (PDOS) was calculated at the vdW-DF/DZP level of theory (check Fig. 5). PDOS analyses indicate that the lowest conduction band (CB) in the spin-up channel of the AF configuration has a predominantly *p* orbital character, stemming from carbon atoms. Simultaneously, the highest valence band (VB) is mostly dominated by *p* orbitals from silicon atoms, despite the fact that the contribution of *p* orbitals from C atoms is still important. In the spin-down channel, *p* orbitals from Si and C atoms and also *d* orbitals from Si atoms contribute equally to the CB. Yet, the VB is controlled by *p* orbitals from C atoms.

In contrast, the M = 1 μ_B state, almost degenerate with the AF configuration, is metallic in the spin-down channel (Fig. 2b), which implies that the band gap previously measured in the same channel and magnetic configuration for the PBL, is completely vanished. On the other hand, the M = 1 μ_B state in the spin-up channel, is also metallic but exhibits a nearly zero band gap above the Fermi level, between the VB crossing the Fermi level and the CB. In this channel, the VB is equally governed by *p* orbitals from carbon and silicon atoms, and the CB in the PDOS is characterized mostly by the sum of the *p* orbitals from Si and C atoms, and *d* orbitals from Si atoms. The NM configuration is also nearly degenerate with the AF one and has a distinctive metal character as the one observed for the NM state of the PBL (Fig. 2c).

The aforementioned data make it clear that the energetic degeneracy (less than 34 meV) among the most stable states, namely AF, NM and M = 1, results in configurations with very dissimilar electronic properties. This is a very different scenario than the one verified for the PBL system where the most stable degenerate magnetic configurations (AF and M = 4 μ_B states) share a semiconductor nature [9]. Most probably, vacancy induced lattice distortions controlled by interaction with the substrate lie at the root of this behavior.

For the M = 2 μ_B configuration, which is only 0.064 eV above the

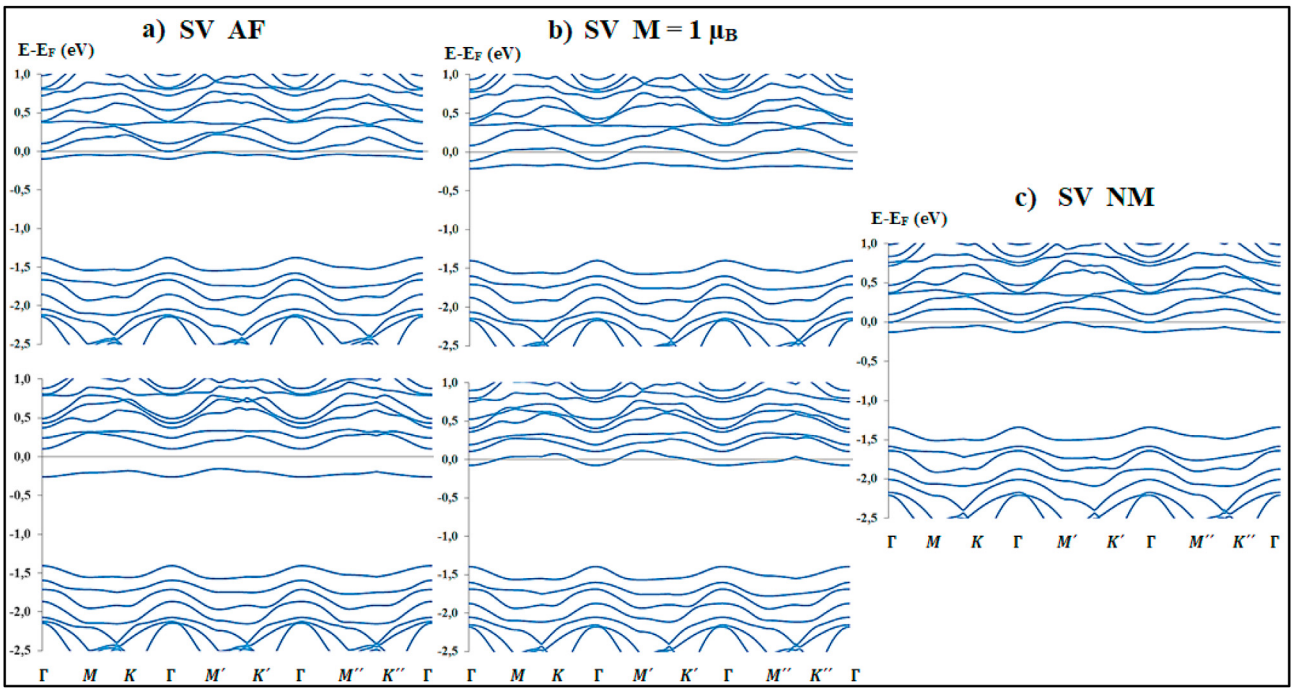

Fig. 2. Band structures determined for the BL with SV over 6H−SiC(0001), at the vdW-DF/DZP level of theory. a) to c): antiferromagnetic, M = 1 μ_B and non-magnetic configurations, respectively. Top and bottom figures correspond to spin up and spin down channels, respectively.

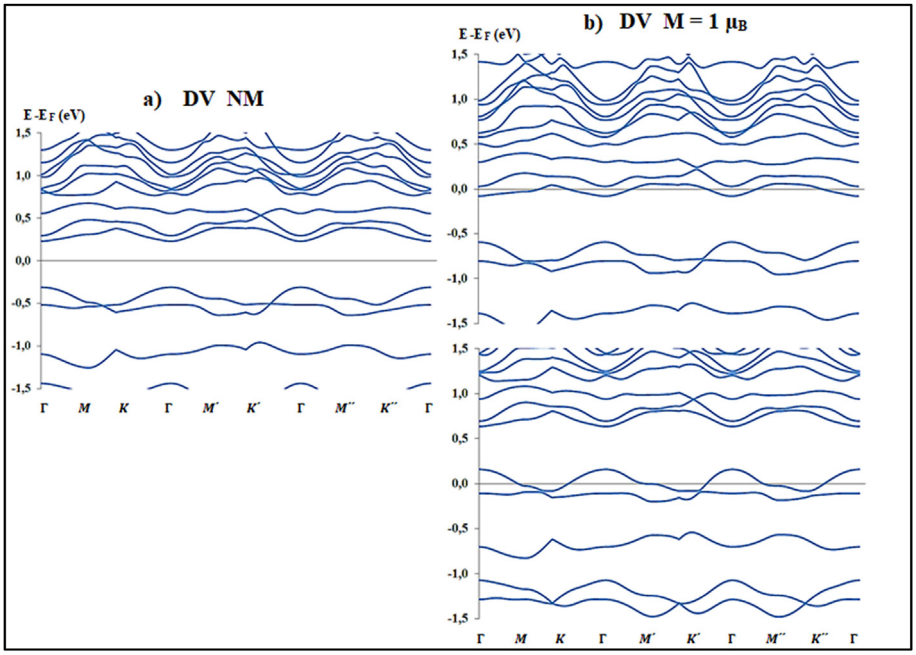

Fig. 3. Band structures determined for the BL with DV over 6H−SiC(0001), at the vdW-DF/DZP level of theory. a) and b): non-magnetic and M = 1 μ_B configurations, respectively. Top and bottom figures correspond to spin up and spin down channels, respectively.

AF state at the vdW-DF/DZP level of theory, the half semimetal behavior verified by the PBL system, is turned into a half metal pattern by virtue of both, a metallic pattern in the spin-up channel with a nearly zero indirect band gap above the Fermi level and an obvious semiconductor pattern in the spin-down channel. Further, the spin-down band in the M = 2 μ_B configuration defines the largest band gap of all defective systems (1.64 eV).

The metallic behavior verified by the PBL system is preserved in the M = 3 μ_B state, even if there is a direct gap (0.16 eV) above the Fermi level at the K point of the Brillouin zone in the spin-up channel and an indirect gap (0.16 eV) below the Fermi level in the spin-down channel, between the VB and the partially filled CB crossing the Fermi level.

In reference to the M = 4 μ_B configuration, the semiconductor character determined for PBL is also maintained upon removal of a single atom in the BL, although the spin-down channel shows a

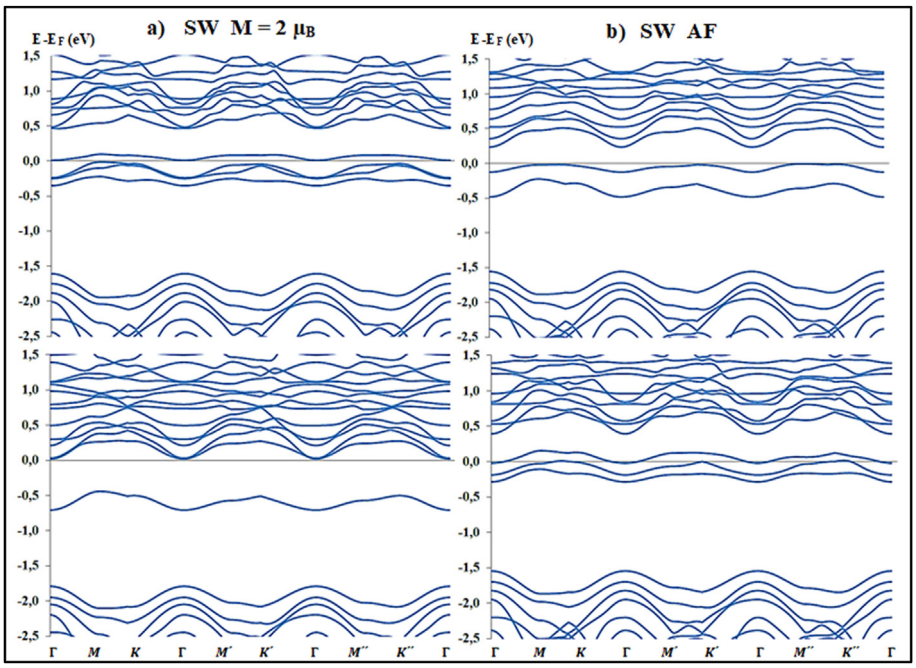

Fig. 4. Band structures determined for the BL with SW over 6H−SiC(0001), at the vdW-DF/DZP level of theory. a) and b): M = 2 μ_B and antiferromagnetic configurations, respectively. Top and bottom figures correspond to spin up and spin down channels, respectively.

Table 1
Band gaps (eV) computed at the vdW-DF/DZP level of theory for different magnetic configurations of the defective BL on 6H−SiC(0001). Previously reported [9] band gaps of perfect SiC-BL system (PBL) are also included for comparison. SV: SiC-BL with single vancancy defect, DV: SiC-BL with divacancy defect, SW: SiC-BL with Stone-Wales defect, NM: non-magnetic, AF: antiferromagnetic.

		PBL	SV	DV	SW
AF	Spin-up	0.19	0.01	–	0.24
	Spin-down	0.19	0.25		M[a]
M = 1 μ_B	Spin-up	M[a]	M[a]	M[a]	M[a]
	Spin-down	0.24	M[a]	M[a]	M[a]
M = 2 μ_B	Spin-up	0.01	M[a]	0.08	0.02
	Spin-down	M[a]	1.64	M[a]	0.45
M = 3 μ_B	Spin-up	M[a]	M[a]	M[a]	M[a]
	Spin-down	M[a]	M[a]	M[a]	M[a]
M = 4 μ_B	Spin-up	0.12	0.13	0.00	0.41
	Spin-down	2.09	0.67	0.44	1.46
NM		M[a]	M[a]	0.54	[a]M

[a] M denotes metal character.

reduction of almost 70% of the band gap when it turns into defective BL. As reported in Refs. [9,30], the spin density distribution in the high magnetic states of SV and PBL (M = 2, 3 and 4 μ_B) is much alike, with both, the carbon atoms of graphene and the Si atoms with DB significantly contributing to the overall magnetic moment. Therefore, one would expect similar electronic properties for these systems.

3.2. BL with a divacancy defect

A metallic behavior is detected in the M = 1 μ_B configuration, just like for the SV system, the difference being that the situation of both channels is reversed, i.e. in the spin-up channel (Fig. 3b) a net metallic behavior was found while the spin down band structure (also metallic) has an indirect band gap of 0.01 eV below the Fermi level, between the VB and the CB crossing the Fermi level.

At the same time, the M = 2 μ_B configuration is half metal in nature, similarly to the PBL case. That is to say, in the spin-up channel a nearly zero band gap (0.08 eV) is verified and in the spin-down channel a metallic character is observed.

As far as the M = 3 μ_B configuration goes, the metallic character present in the PBL and SV systems is conserved. Nonetheless, a direct band gap above the Fermi level is found (0.05 eV) in the spin-up channel, between the VB crossing the Fermi level and the CB and a larger indirect band gap (0.40 eV) is seen below the Fermi level, in the spin-down channel.

In line with the PBL and SV systems, a semiconductor character is found in both channels of the M = 4 μ_B configuration. It is also worth noting that in the spin-up channel of this state, a graphene-like Dirac cone is present at the K' point of the Brillouin zone at the Femi level.

The electronic structures of the M = 2 μ_B, M = 3 μ_B and M = 4 μ_B configurations in the spin-up channel correspond to a doped *n*-type which means that the Fermi level has been shifted upward into the CB, comparing with the NM state. In this case, the increase in magnetism results in a more characteristic *n*-type doping character. On the other hand, the electronic structures of all the magnetic configurations in the spin-down channel are *p*-type, with a very similar Fermi energy shifting into the VB.

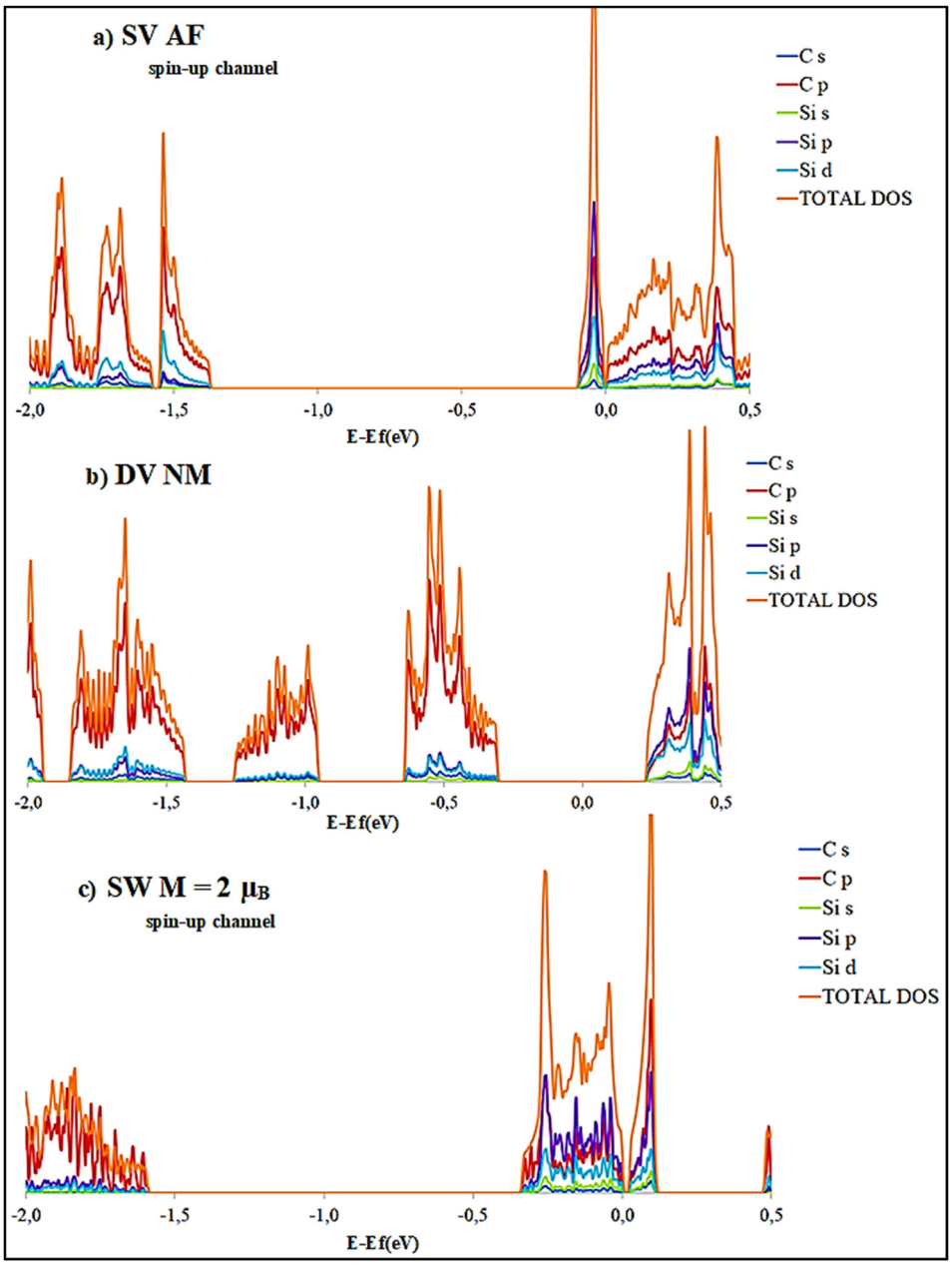

Fig. 5. Projected density of states calculated at the vdW-DF/DZP level of theory.

3.3. BL with a Stone-Wales defect

Band structures for the SW defective SiC-BL systems are shown in Fig. 4. The M = 2 μ_B magnetic state is a semiconductor with a nearly zero indirect band gap in the spin-up channel (Fig. 4a); this is in fact a recurrence for this magnetic state in almost all studied systems (the exception is SV which presents a virtually zero gap above the Fermi level). In this channel, the CB presents mostly a *p* orbital character from C atoms whereas the VB is equally dominated by *p* orbitals from Si and C atoms, even though *d* orbitals from Si atoms also make a significant contribution (Fig. 5). For the spin-down channel, the energy band gap is larger (0.45 eV). In this case, the VB is located much below the Fermi level and a clear *p* orbital character from C atoms is observed in said band. As for the CB in the spin-down channel, *d* and also *p* orbitals from Si atoms mark this band. It should be stressed that, according to the PDOS analysis, for all models, *d* orbitals from Si atoms always make important contributions to the CB in the spin-down channels of the most stable magnetic configurations.

The AF state, nearly energetically degenerate with the M = 2 μ_B state, displays a band gap of 0.24 eV in both channels. However, the band structures at the Fermi region are quite different (see Fig. 4b). The band gap is above the Fermi level in the spin-down channel (the system is metallic in this channel); the VB crosses the Fermi level with a *p* orbital character acquired from Si and C atoms (principally C atoms from the BL). Concomitantly, in the spin-up channel, this band lies below the Fermi level across the studied path in the Brillouin zone. It approaches this level at the *MK*, *MḰ*; *MḰ́* lines and is mostly characterized by *p* orbitals from Si atoms. By contrast, in both channels the CB has a similar behavior, controlled evenly by *p* orbitals from Si and C atoms.

On the other hand, the M = 1 μ_B configuration is metallic. It is

noteworthy that all SV, DV and SW systems are metallic in the M = 1 μB configuration, i.e. the band gap detected for the PBL system in the very same configuration vanishes for the defective systems.

A metallic character was apparent in the M = 3 μ_B state, the same as the M = 3 μ_B configurations of PBL, SV and DV systems. Nevertheless, there is a band gap of 0.43 eV above the Fermi level in the spin-up channel of this magnetic configuration.

In agreement with the results pertaining to the PBL, SV and DV systems, the M = 4 μ_B configuration of the SW system is a semiconductor. However, a diminution of the band gap in the spin-down channel and an increase in the spin-up channel, comparing to the PBL system, was found due to the presence of the SW defect. The decrease in the spin-down channel is lower than the one observed with one and two vacancies.

The largest band gap among all the magnetic configurations of the SW system correspond to the spin down channel in the M = 4 μ_B state (1.46 eV). On the contrary, the NM state has a distinctive metal character just like the one seen for the rest of the NM states, with the exception of the DV defective system.

3.4. Effective mass calculations

The effective mass (m^*) of a semiconductor can be calculated by fitting the actual E vs. k diagram around the CB minimum or the VB maximum to a parabolic curve. In this approximation, electrons and holes are expected to behave as free particles with relatively low energies and may be treated using the so called parabolic band approximation given by the equation:

$$m^* = \hbar^2 \cdot \left(\frac{\partial^2 E(k)}{\partial k^2} \right)^{-1} \quad (1)$$

Most semiconductors can be described as having one CB minimum and one VB maximum. Nevertheless, it is often the case that the bottom of the CB has more than one minimum at different points in the Brillouin zone with exactly the same energy. It is said that there are multiple valleys in the band structure. Such a situation takes place due to the symmetry of the crystal. Following the above mentioned rationale, the calculated electron (m_e^*)and hole (m_h^*) effective masses of perfect and defective SiC-BL systems are gathered in Tables 2 and 3. As of yet, there are no experimental data available for comparison. Due to the symmetry of these models, not only multiple energetically equivalent valleys are observed, but also equivalent crests. When more than one equivalent minimum or maximum occurred along the ΓM, KΓM′, KΓM′and KΓ′ lines, an individual effective mass calculation following equation (1) was performed for each of them.

For the PBL system, the equivalent minima and maxima are located at the same point, namely Γ, only in the case of the M = 4 μB configuration. At this point, we remind the reader that the most stable magnetic configurations for the PBL were the AF and the M = 4 μB ones. Specifically for the AF state of the PBL system, the electron effective masses fitted to the four equivalent minima are very similar for the spin-up and spin-down channels: values range from 1.21 to 1.32 m_0 ($m_0 = 9,11 \times 10^{-31} kg$). Contrariwise, the maximum is reached at a single point of the VB and presents a very high hole effective mass of approximately $m_h^* = 10.8\ m_0$ in both channels. This is reasonable because the spin-up and spin-down channels in the antiferromagnetic state are nearly degenerate (the band structures are very similar [9] and present an indirect band gap of about 0.2 eV, at the vdW-DF level of theory).

As regards the M = 4 μB configuration of the PBL system, the smaller band gap in the spin-up channel (in comparison with the band gap in the spin-up band structure of the AF state) is reflected in smaller electron effective masses. In the same way, the larger band gap in the spin-down channel is translated into the increase of electron effective masses. Conversely, the hole effective masses in the M = 4 μB configuration of the PBL system do not follow directly the band gap size line, probably due to spin-orbit splitting effect seen in the valence bands. This effect is lost in the band structure of defective systems. It is straightforward that the increase of the magnetic moment in the PBL system yields smaller hole effective masses.

The removal of a single carbon atom in the BL generates structural distortions throughout the entire system, resulting in a clear anisotropy (according to the studied path in the Brillouin zone) in the band structures of the SV system that is reflected in the effective

Table 2
Electron (m_e^*) and hole (m_h^*) effective masses in m_0 units determined for different magnetic configurations of the SiC-BL with SV and for the perfect SiC-BL system, at the vdW-DF/DZP level of theory, along the ΓM, ΓM′, KΓM′and KΓ′ paths in the Brillouin zone.

			m_e^* ΓM	m_e^* KΓM′	m_e^* KΓ′M′	m_e^* KΓ′	m_h^* ΓM	m_h^* KΓM′	m_h^* KΓ′M′	m_h^* KΓ′
PBL	AF	Spin-up	**1.31**	**1.26**	**1.21**	**1.32**	**10.78**			
		Spin-down	**1.31**	**1.26**	**1.26**	**1.32**	**10.86**			
	M = 1 μ_B	Spin-up	-							
		Spin-down	**0.88**	**1.30**	**1.31**	**0.83**	**7.22**			
	M = 2 μ_B	Spin-up	**1.11**				**1.06**			
		Spin-down	-							
	M = 3 μ_B	Spin-up	-							
		Spin-down	-							
	M = 4 μ_B	Spin-up	**0.84**	**0.71**	**0.81**	**0.79**	**1.52**	**1.43**	**1.51**	**1.51**
		Spin-down	**1.10**	**1.44**	**1.53**	**1.11**	**0.86**	**0.71**	**0.67**	**0.83**
	NM		-							
SV	AF	Spin-up	**1.05**	**0.92**	**2.04**	**1.57**	**2.61**			
		Spin-down	**0.99**	**1.49**	**1.11**	**0.84**	**2.18**			
	M = 1 μ_B	Spin-up	-							
		Spin-down	-							
	M = 2 μ_B	Spin-up	-							
		Spin-down	**1.01**	**1.01**	**1.81**	**1.50**	**0.79**	**0.65**	**1.23**	**1.23**
	M = 3 μ_B	Spin-up	-							
		Spin-down	-							
	M = 4 μ_B	Spin-up	**1.78**	**2.89**	**1.20**	**1.14**	**1.13**			
		Spin-down	**1.09**				**1.01**	**0.67**	**1.05**	**1.40**
	NM		–							

Table 3
Electron (m_e^*) and hole (m_h^*) effective masses in m_0 units determined for different magnetic configurations of the SiC-BL with DV and SW defects, at the vdW-DF/DZP level of theory, along the ΓM, $\Gamma M'$, $K\Gamma M'$and $K'\Gamma$ paths in the Brillouin zone.

			m_e^* ΓM	m_e^* $K\Gamma M'$	m_e^* $K'\Gamma M'$	m_e^* $K'\Gamma$	m_h^* ΓM	m_h^* $K\Gamma M'$	m_h^* $K'\Gamma M'$	m_h^* $K'\Gamma$
DV	AF		-							
	M = 1 μ_B	Spin-up	-							
		Spin-down	-							
	M = 2 μ_B	Spin-up	**1.79**	**1.02**	**0.82**	**1.46**	**2.31**			
		Spin-down	-							
	M = 3 μ_B	Spin-up	-							
		Spin-down	-							
	M = 4 μ_B	Spin-up	**0.06**				**0.06**			
		Spin-down	**1.00**				**0.44**			
	NM		**1.54**	**1.12**	**0.91**	**1.34**	**1.84**	**1.36**	**1.06**	**1.58**
SW	AF	Spin-up	**0.63**	**0.47**	**0.69**	**0.79**	**7.84**			
		Spin-down	-							
	M = 1 μ_B	Spin-up	-							
		Spin-down	-							
	M = 2 μ_B	Spin-up	**2.47**	**1.88**	**1.61**	**2.25**	**2.23**			
		Spin-down	**0.64**	**0.51**	**0.40**	**0.73**	**1.05**			
	M = 3 μ_B	Spin-up	-							
		Spin-down	-							
	M = 4 μ_B	Spin-up	**8.05**	**2.19**	**1.15**	**3.00**	**9.80**			
		Spin-down	**0.76**	**1.04**	**1.38**	**0.88**	**0.92**	**1.01**	**1.09**	**1.00**
	NM		-							

masses. Effectively, while in the AF configuration all the valleys occur at the gamma point, m_e^* values vary from 0.92 to 2.04 m_0 in the spin-up channel, and from 0.84 to 1.49 m_0 in the spin-down channel. Concerning the CB, the maximum is reached at only one point of the path, but the value of m_h^* in the antiferromagnetic PBL is reduced by 76−80%. In this manner, there is a drop in the values of the hole effective masses from PBL to SV. The lack of a C−Si interface bond in the latter system, which would reduce the scattering effect, could account for this distinction.

As for the most stable configuration (NM) of the DV system, as many as four m_e^* and four m_h^* were calculated at the vdW-DF level of theory. Very similar electron effective masses were obtained for the M = 2 μB and the NM configurations even though the band gaps are very different in both configurations (see Tables 1 and 3).

In the M = 4 μB configuration of the DV system, the maximum and minimum are achieved at only one point of the path $(K)'$. In the spin-up channel (comprising the graphene-like Dirac cone previously mentioned) the smallest effective mass of all defective systems is verified (0.06 m_0 for both electron and hole effective masses).

Smaller effective masses (m_e^* varying from 0.47 to 0.79 m_0 and a value of 7.84 m_0 for m_h^*) were also measured for the AF state of the SW system in comparison with the same state of the PBL system.

For the M = 2 μB stable state of the SW system, m_e^* values ranged from 1.61 to 2.47 m_0 in the spin-up channel and smaller effective masses were found in the spin-down one (0.40−0.73 m_0). Also m_h^* in spin-up and down channels measured 2.23 and 1.05 m_0, respectively.

The largest hole effective mass among all studied systems corresponds to the spin-up channel of the M = 4 μB configuration of the SW system. This is likely caused by the flat VB which makes the parabolic approximation not ideal for this model.

The effective masses in the spin-down channel of the M = 4 μB configuration of the SW system are smaller in general than the ones obtained for the same magnetic configuration of the PBL system.

4. Conclusions

In this paper, first principle calculations were applied to study the electronic properties of SiC-BL defective systems, considering different magnetic states for each of them. Structural local reconstruction at the vicinity of defects as well as spin polarization of both, silicon dangling bonds in the top bilayer SiC and nearby carbons from the BL, give rise to energetically degenerate magnetic states displaying electronic properties completely apart. This is in sharp disagreement with previously reported results for the PBL which suggested that the most stable degenerate magnetic configurations share a semiconductor nature.

In relation to the SV defective model where three different magnetic states turned out to be degenerate, semiconductor, half-metallic and metallic characters are observed. For the DV system, the introduction of two vacancies in the carbon network of the PBL causes loss of magnetism and renders the system semiconductor, opening a band gap of 0.54 eV. In the case of the SW defective system, three out of six magnetic states display a different electronic nature as compared with the non-defective system. Added to this, the two degenerate magnetic states behave either as half-metal or semiconductor, in the presence of a SW defect.

Defects on the BL do change the size of the band gaps, examples of which were provided above. Effective masses are also altered. In particular, hole effective masses decay upon removal of one and two carbon atoms, bearing in mind the most stable magnetic states. It is common knowledge that the size of the effective mass affects directly the electron mobility since both magnitudes are inversely proportional. Based on our results, we suggest that the presence of defects in the BL may increase the carrier mobility providing a potential application in high-speed electric devices. However current directions should be carefully selected. Otherwise, too small electron mobilities may result, hampering the application of these models.

Declaration of competing interest

The authors declare that they have no known competing financial interests or personal relationships that could have appeared to influence the work reported in this paper.

Acknowledgments

The authors thank PEDECIBA Química, CAP and ANII Uruguayan institutions for financial support.

References

[1] P.R. Wallace, The band theory of graphite, Phys. Rev. 71 (1947) 622–634, https://doi.org/10.1103/PhysRev.71.622.

[2] K.S. Novoselov, A.K. Geim, S.V. Morozov, D. Jiang, Y. Zhang, S.V. Dubonos, I.V. Grigorieva, A.A. Firsov, Electric field effect in atomically thin carbon films, Science 306 (2004) 666–669, https://doi.org/10.1126/science.1102896.

[3] A.K. Geim, K.S. Novoselov, The rise of graphene, Nat. Mater. 6 (2007) 183–191, https://doi.org/10.1038/nmat1849.

[4] K. Kim, J.-Y. Choi, T. Kim, S.-H. Cho, H.-J. Chung, A role for graphene in silicon-based semiconductor devices, Nature 479 (2011) 338–344, https://doi.org/10.1038/nature10680.

[5] K.S. Novoselov, V.I. Fal'ko, L. Colombo, P.R. Gellert, M.G. Schwab, K. Kim, A roadmap for graphene, Nature 490 (2012) 192–200, https://doi.org/10.1038/nature11458.

[6] J. Liu, Y. Xue, M. Zhang, L. Dai, Graphene-based materials for energy applications, MRS Bull. 37 (2012) 1265–1272, https://doi.org/10.1557/mrs.2012.179.

[7] C. Berger, Z. Song, T. Li, X. Li, A.Y. Ogbazghi, R. Feng, Z. Dai, A.N. Marchenkov, E.H. Conrad, P.N. First, et al., Ultrathin epitaxial graphite: 2D electron gas properties and a route toward graphene-based nanoelectronics, J. Phys. Chem. 108 (2004) 19912–19916, https://doi.org/10.1021/jp040650f.

[8] G.R. Yazdi, T. Iakimov, R. Yakimova, Epitaxial graphene on SiC: a review of growth and characterization, Crystals 6 (2016) 53–97, https://doi.org/10.3390/cryst6050053.

[9] C.P. Huelmo, P.A. Denis, Unraveling the electromagnetic structure of the epitaxial graphene buffer layer, J. Phys. Condens. Matter 31 (2019) 435001–435011, https://doi.org/10.1088/1361-648X/ab2ee2.

[10] D. Usachov, O. Vilkov, A. Grüneis, D. Haberer, A. Fedorov, V.K. Adamchuk, A.B. Preobrajenski, P. Dudin, A. Barinov, M. Oehzelt, et al., Nitrogen-doped graphene: efficient growth, structure, and electronic properties, Nano Lett. 11 (2011) 5401–5407, https://doi.org/10.1021/nl2031037.

[11] L. Lin, J. Li, Q. Yuan, Q. Li, J. Zhang, L. Sun, D. Rui, Z. Chen, K. Jia, M. Wang, et al., Nitrogen cluster doping for high-mobility/conductivity graphene films with millimeter-sized domains, Sci. Adv. 5 (2019), eaaw8337, https://doi.org/10.1126/sciadv.aaw8337.

[12] P.A. Denis, C.P. Huelmo, F. Iribarne, Theoretical characterization of sulfur and nitrogen dual-doped graphene, Comput. Theor. Chem. 1049 (2014) 13–19, https://doi.org/10.1016/j.comptc.2014.08.023.

[13] H.C. Wu, M. Abid, Y.C. Wu, C.Ó. Coileáin, A. Syrlybekov, J.F. Han, C.L. Heng, H. Liu, M. Abid, I. Shvets, Enhanced shubnikov-de haas oscillation in nitrogen-doped graphene, ACS Nano 9 (2015) 7207–7214, https://doi.org/10.1021/acsnano.5b02020.

[14] P.A. Denis, C.P. Huelmo, A.S. Martins, Band gap opening in dual doped monolayer graphene, J. Phys. Chem. C 120 (2016) 7103–7112, https://doi.org/10.1021/acs.jpcc.5b11709.

[15] P.A. Denis, C.P. Huelmo, F. Iribarne, On the band gaps and effective masses of mono and dual doped monolayer graphene, Comput. Mater. Sci. 137 (2017) 20–29, https://doi.org/10.1016/j.commatsci.2017.05.006.

[16] H. He, K.H. Kim, A. Danilov, D. Montemurro, L. Yu, Y.W. Park, F. Lombardi, T. Bauch, K. Moth-Poulsen, T. Iakimov, et al., Uniform doping of graphene close to the Dirac point by polymer-assisted assembly of molecular dopants, Nat. Commun. 9 (2018) 3956, https://doi.org/10.1038/s41467-018-06352-5.

[17] W. Chen, S. Chen, D.C. Qi, X.Y. Gao, A.T.S. Wee, Surface transfer p-type doping of epitaxial graphene, J. Am. Chem. Soc. 129 (2007) 10418–10422, https://doi.org/10.1021/ja071658g.

[18] C. Coletti, C. Riedl, D.S. Lee, B. Krauss, L. Patthey, K. von Klitzing, J.H. Smet, U. Starke, Charge neutrality and band-gap tuning of epitaxial graphene on SiC by molecular doping, Phys. Rev. B 81 (2010) 235401–235408, https://doi.org/10.1103/PhysRevB.81.235401.

[19] H. Pinto, R. Jones, J.P. Goss, P.R. Briddon, p-type doping of graphene with F4-TCNQ, J. Phys. Condens. Matter 21 (2009) 402001–402003, https://doi.org/10.1088/0953-8984/21/40/402001.

[20] F. Cervantes-Sodi, G. Csányi, S. Piscanec, A.C. Ferrari, Edge-functionalized and substitutionally doped graphene nanoribbons: electronic and spin properties, Phys. Rev. B 77 (2008) 165427–165438, https://doi.org/10.1103/PhysRevB.77.165427.

[21] H.Y. Mao, Y.H. Lu, J.D. Lin, S. Zhong, A.T.S. Wee, W. Chen, Manipulating the electronic and chemical properties of graphene via molecular functionalization, Prog. Surf. Sci. 88 (2013) 132–159, https://doi.org/10.1016/j.progsurf.2013.02.001.

[22] M.M. Ugeda, I. Brihuega, F. Hiebel, P. Mallet, Electronic and structural characterization of divacancies in irradiated graphene, Phys. Rev. B 85 (2012) 121402–121406, https://doi.org/10.1103/PhysRevB.85.121402.

[23] D. Teweldebrhan, A.A. Balandin, Modification of graphene properties due to electron-beam irradiation, Appl. Phys. Lett. 94 (2009) 13101–13103, https://doi.org/10.1063/1.3062851.

[24] P. Ruffieux, O. Gröning, P. Schwaller, L. Schlapbach, P. Gröning, Hydrogen atoms cause long-range electronic effects on graphite, Phys. Rev. Lett. 84 (2000) 4910–4913, https://doi.org/10.1103/PhysRevLett.84.4910.

[25] H.-g. Jee, K.-H. Jin, J.-H. Han, H.-N. Hwang, S.-H. Jhi, Y.D. Kim, C.-C. Hwang, Controlling the self-doping of epitaxial graphene on SiC via Ar ion treatment, Phys. Rev. B 84 (2011) 75457–75461, https://doi.org/10.1103/PhysRevB.84.075457.

[26] B.W. Smith, D.E. Luzzi, Electron irradiation effects in single wall carbon nanotubes, J. Appl. Phys. 90 (2001) 3509–3515, https://doi.org/10.1063/1.1383020.

[27] A.V. Krasheninnikov, P.O. Lehtinen, A.S. Foster, R.M. Nieminen, Bending the rules: contrasting vacancy energetics and migration in graphite and carbon nanotubes, Chem. Phys. Lett. 418 (2006) 132–136, https://doi.org/10.1016/j.cplett.2005.10.106.

[28] P.A. Denis, R. Faccio, F. Iribarne, How is the stacking interaction of bilayer graphene affected by the presence of defects? Comput. Theor. Chem. 995 (2012) 1–7, https://doi.org/10.1016/j.comptc.2012.06.014.

[29] S.T. Skowron, I.V. Lebedeva, A.M. Popov, E. Bichoutskaia, Energetics of atomic scale structure changes in graphene, Chem. Soc. Rev. 44 (2015) 3143–3176, https://doi.org/10.1039/C4CS00499J.

[30] C.P. Huelmo, M.G. Menezes, P.A. Denis, R.B. Capaz, Structural and magnetic properties of a defective graphene buffer layer grown on SiC(0001): a DFT study, Phys. Chem. Chem. Phys. 22 (2020) 16096–16106, https://doi.org/10.1039/D0CP02167A.

[31] Y. Kim, J. Ihm, E. Yoon, G.-D. Lee, Dynamics and stability of divacancy defects in graphene, Phys. Rev. B 84 (2011) 75445–75449, https://doi.org/10.1103/PhysRevB.84.075445.

[32] G.-D. Lee, C.Z. Wang, E. Yoon, N.-M. Hwang, D.-Y. Kim, K.M. Ho, Diffusion, coalescence, and reconstruction of vacancy defects in graphene layers, Phys. Rev. Lett. 95 (2005) 205501–205504, https://doi.org/10.1103/PhysRevLett.95.205501.

[33] F. Banhart, J. Kotakoski, A.V. Krasheninnikov, Structural defects in graphene, ACS Nano 5 (2011) 26–41, https://doi.org/10.1021/nn102598m.

[34] X.-L. Ye, J. Cai, X.-D. Yang, X.-Y. Tang, Z.-Y. Zhou, Y.-Z. Tan, S.-Y. Xie, L.-S. Zheng, Quantifying defect-enhanced chemical functionalization of single-layer graphene and its application in supramolecular assembly, J. Mater. Chem. 5 (2017) 24257–24262, https://doi.org/10.1039/C7TA07612F.

[35] Y.-H. Zhang, Y.-B. Chen, K.-G. Zhou, C.-H. Liu, J. Zeng, H.-L. Zhang, Y. Peng, Improving gas sensing properties of graphene by introducing dopants and defects: a first-principles study, Nanotechnology 20 (2009) 185504–185511, https://doi.org/10.1088/0957-4484/20/18/185504.

[36] O. Cretu, A.V. Krasheninnikov, J.A. Rodrıguez-Manzo, L. Sun, R.M. Nieminen, F. Banhart, Migration and localization of metal atoms on strained graphene, Phys. Rev. Lett. 105 (2010) 196102–196105, https://doi.org/10.1103/PhysRevLett.105.196102.

[37] Y. Orimoto, K. Otsuka, K. Yagyu, H. Tochihara, T. Suzuki, Y. Aoki, Theoretical study of Cu intercalation through a defect in zero-layer graphene on SiC surface, J. Phys. Chem. C 121 (2017) 7294–7302, https://doi.org/10.1021/acs.jpcc.7b00314.

[38] A. Markevich, R. Jones, S. Öberg, M.J. Rayson, J.P. Goss, P.R. Briddon, First-principles study of hydrogen and fluorine intercalation into graphene-SiC(0001) interface, Phys. Rev. B 86 (2012) 45453–45461, https://doi.org/10.1103/PhysRevB.86.045453.

[39] A.J. Pak, E.P. Gyeong, S. Hwang, Tailoring the performance of graphene-based supercapacitors using topological defects, A Theoretical Assessment, Carbon 68 (2014) 734–741, https://doi.org/10.1016/j.carbon.2013.11.057.

[40] H.A. Mizes, J.S. Foster, Long-range electronic perturbations caused by defects using scanning tunneling microscopy, Science 244 (1989) 559–562, https://doi.org/10.1126/science.244.4904.559.

[41] T.O. Wehling, S. Yuan, A.I. Lichtenstein, A.K. Geim, M.I. Katsnelson, Resonant scattering by realistic impurities in graphene, Phys. Rev. Lett. 105 (2010) 56802–56805, https://doi.org/10.1103/PhysRevLett.105.056802.

[42] A. Lherbier, S.M.-M. Dubois, X. Declerck, Y.-M. Niquet, S. Roche, J.-C. Charlier, Transport properties of graphene containing structural defects, Phys. Rev. B 86 (2012) 75402–75419, https://doi.org/10.1103/PhysRevB.86.075402.

[43] J. Lahiri, Y. Lin, P. Bozkurt, I.I. Oleynik, M. Batzill, An extended defect in graphene as a metallic wire, Nat. Nanotechnol. 5 (2010) 326–329, https://doi.org/10.1038/nnano.2010.53.

[44] O.V. Yazyev, S.G. Louie, Electronic transport in polycrystalline graphene, Nat. Mater. 9 (2010) 806–809, https://doi.org/10.1038/nmat2830.

[45] M. Dion, H. Rydberg, E. Schröder, D.C. Langreth, B.I. Lundqvist, Phys. Rev. Lett. 92 (2004) 246401–246404, https://doi.org/10.1103/PhysRevLett.92.246401.

[46] P. Ordejón, E. Artacho, J.M. Soler, Self-consistent order-N density-functional calculations for very large systems, Phys. Rev. B 53 (1996) R10441–R10444, https://doi.org/10.1103/PhysRevB.53.R10441.

[47] J.M. Soler, E. Artacho, J.D. Gale, A. García, J. Junquera, P. Ordejón, D. Sánchez-Portal, The SIESTA method for ab initio order-N materials simulation, J. Phys. Condens. Matter 14 (2002) 2745–2779, https://doi.org/10.1088/0953-8984/14/11/302.

[48] I. Hamada, M. Otani, Comparative van der Waals density-functional study of graphene on metal surface, Phys. Rev. B 82 (2010) 153412, https://doi.org/10.1103/PhysRevB.82.153412.

[49] N. Troullier, J.L. Martins, Efficient pseudopotentials for plane-wave calculations, Phys. Rev. B 43 (1991) 1993–2006, https://doi.org/10.1103/PhysRevB.43.1993.

[50] S. Zhao, Q. Wu, J. Pi, J. Liu, J. Zheng, S. Hou, J. Wei, R. Li, H. Sadeghi, Y. Yang, et al., Cross-plane transport in a single-molecule two-dimensional van der Waals heterojunction, Sci. Adv. 6 (2020), eaba6714, https://doi.org/10.1126/sciadv.aba6714.

[51] W. Hu, Y. Huang, X. Qin, L. Lin, E. Kan, X. Li, C. Yang, J. Yang, Room-temperature magnetism and tunable energy gaps in edge-passivated zigzag graphene quantum dots, NPJ 2D Mater. Appl. 3 (2019) 17, https://doi.org/

10.1038/s41699-019-0098-2.
[52] B. Huang, H.J. Xiang, S.-H. Wei, Controlling doping in graphene through a SiC substrate: a first-principles study, Phys. Rev. B 83 (2011) 161405−161408, https://doi.org/10.1103/PhysRevB.83.161405.
[53] M. Ridene, C.S. Kha, C.F.J. Flipse, Role of silicon dangling bonds in the electronic properties of epitaxial graphene on silicon carbide, Nanotechnology 27 (2016) 125705−125711, https://doi.org/10.1088/0957-4484/27/12/125705.
[54] T. Jayasekera, B.D. Kong, K.W. Kim, M.B. Nardelli, Band engineering and magnetic doping of epitaxial graphene on SiC (0001), Phys. Rev. Lett. 104 (2010) 146801−146804, https://doi.org/10.1103/PhysRevLett.104.146801.
[55] T. Cavallucci, V. Tozzini, Intrinsic structural and electronic properties of the bufer layer on silicon carbide unraveled by density functional theory, Sci. Rep. 8 (2018) 13097−13106.
[56] F. Varchon, R. Feng, J. Hass, X. Li, B. Ngoc Nguyen, C. Naud, P. Mallet, J.-Y. Veuillen, C. Berger, E.H. Conrad, et al., Electronic structure of epitaxial graphene layers on SiC: effect of the substrate, Phys. Rev. Lett. 99 (2007) 126805−126808, https://doi.org/10.1103/PhysRevLett.99.126805.
[57] S. Kim, J. Ihm, H.J. Choi, Y.-W. Son, Origin of anomalous electronic structures of epitaxial graphene on silicon carbide, Phys. Rev. Lett. 100 (2008) 176802−176805, https://doi.org/10.1103/PhysRevLett.100.176802.
[58] C.P. Huelmo, P.A. Denis, Silicon carbide induced doping of graphene: a new potential synthetic route for SiC3 siligraphene, J. Phys. Chem. C 123 (2019) 30341−30350, https://doi.org/10.1021/acs.jpcc.9b07978.